Radiative impacts of Californian marine low clouds on North Pacific climate

Ayumu Miyamoto[1], Hisashi Nakamura[2,3], Shang-Ping Xie[1], Takafumi Miyasaka[2], and Yu Kosaka[2]

[1]Scripps Institution of Oceanography, University of California San Diego
[2]Research Center for Advanced Science and Technology, The University of Tokyo
[3]Japan Agency for Marine-Earth Science and Technology

March 26, 2023

Abstract

The northeastern Pacific climate system is featured by an extensive low-cloud deck off California on the southeastern flank of the subtropical high that accompanies intense northeasterly trades and relatively low sea surface temperatures (SSTs). This study investigates climatic impacts of the low-cloud deck by turning low-cloud radiative forcing on and off only within the subtropical northeastern Pacific in a coupled atmosphere-ocean model. The low-cloud radiative forcing causes a local SST decrease of up to 3ºC on an annual average, with the response extending southwestward through the wind-evaporation-SST (WES) feedback. The SST decrease peaks in summer under the seasonally enhanced insolation and the seasonally shallow ocean mixed layer. The lowered SST suppresses deep-convective precipitation that would otherwise occur in the absence of the low-cloud deck. The resultant anomalous diabatic cooling induces a surface anticyclonic response in summer and autumn as a baroclinic Matsuno-Gill pattern. On its equatorward flank, the enhanced trade winds further cool SST as the WES feedback, leading to the southwest propagation of the coupled response. The enhanced trades accompany the intensified upper-tropospheric westerlies, strengthening the vertical wind shear that, together with the lowered SST, acts to shield Hawaii from powerful hurricanes. On the basin scale, the anticyclonic surface wind response accelerates the North Pacific subtropical ocean gyre to speed up the Kuroshio by as much as 30%. SST thereby increases along the Kuroshio and its extension, intensifying upward turbulent heat fluxes from the ocean to increase precipitation.

Radiative impacts of Californian marine low clouds on North Pacific climate

Ayumu Miyamoto,[a] Hisashi Nakamura,[b,c] Shang-Ping Xie,[a] Takafumi Miyasaka,[b] and Yu Kosaka,[b]

[a] *Scripps Institution of Oceanography, University of California San Diego, La Jolla, California, USA* [b] *Research Center for Advanced Science and Technology, The University of Tokyo, Tokyo, Japan*

[c] *Japan Agency for Marine-Earth Science and Technology, Yokohama, Japan*

Manuscript submitted to Journal of Climate on March 14th, 2023

Corresponding author: Ayumu Miyamoto, aymiyamoto@ucsd.edu

ABSTRACT: The northeastern Pacific climate system is featured by an extensive low-cloud deck off California on the southeastern flank of the subtropical high that accompanies intense northeasterly trades and relatively low sea surface temperatures (SSTs). This study investigates climatic impacts of the low-cloud deck by turning low-cloud radiative forcing on and off only within the subtropical northeastern Pacific in a coupled atmosphere-ocean model. The low-cloud radiative forcing causes a local SST decrease of up to 3°C on an annual average, with the response extending southwestward through the wind-evaporation-SST (WES) feedback. The SST decrease peaks in summer under the seasonally enhanced insolation and the seasonally shallow ocean mixed layer. The lowered SST suppresses deep-convective precipitation that would otherwise occur in the absence of the low-cloud deck. The resultant anomalous diabatic cooling induces a surface anticyclonic response in summer and autumn as a baroclinic Matsuno-Gill pattern. On its equatorward flank, the enhanced trade winds further cool SST as the WES feedback, leading to the southwest propagation of the coupled response. The enhanced trades accompany the intensified upper-tropospheric westerlies, strengthening the vertical wind shear that, together with the lowered SST, acts to shield Hawaii from powerful hurricanes. On the basin scale, the anticyclonic surface wind response accelerates the North Pacific subtropical ocean gyre to speed up the Kuroshio by as much as 30%. SST thereby increases along the Kuroshio and its extension, intensifying upward turbulent heat fluxes from the ocean to increase precipitation.

1. Introduction

Over each of the subtropical oceans, large-scale surface winds are characterized by subtropical highs (e.g., Rodwell and Hoskins 2001; Seager et al. 2003; Miyasaka and Nakamura 2005, 2010; Nakamura et al. 2010; Miyamoto et al. 2022b). To the east of a subtropical high, enhanced lower-tropospheric stability due to mid-tropospheric subsidence and low sea surface temperature (SST) promotes abundant low clouds (e.g., Klein and Hartmann 1993; Wood and Bretherton 2006; Miyamoto et al. 2018). Since low clouds reflect a substantial fraction of incoming shortwave radiation, they are crucial in Earth energy budget (Hartmann et al. 1992) and its perturbations such as global warming (Bony et al. 2005; Zelinka et al. 2020).

The cooling effect of low clouds is important in regional climate through air-sea interactions. Reflecting insolation, low clouds act to reinforce the underlying low SST. This results in stronger lower-tropospheric stability, which facilitates low-cloud formation. This local feedback, known as positive low cloud-SST feedback, has been identified as crucial air-sea coupled feedback over the eastern subtropical oceans (e.g., Norris and Leovy 1994; Clement et al. 2009; Myers et al. 2018; Yang et al. 2022).

Although the local radiative impacts of low clouds are widely accepted, their non-local effect has not been understood well. As low SST over the eastern subtropical oceans is important in maintaining the subtropical high (Seager et al. 2003; Miyasaka and Nakamura 2005, 2010), SST cooling by low clouds is suggested to reinforce the subtropical high. They can also reinforce the subtropical high through cloud-top longwave cooling (Miyasaka and Nakamura 2005, 2010). Strengthened trade winds associated with the enhanced subtropical high act to cool the SST by promoting evaporation from the ocean. This wind-evaporation-SST (WES) feedback (Xie and Philander 1994) propagates westward, yielding remote influence on the equatorial oceans (Xie et al. 2007; Yang et al. 2022). Nevertheless, it has been controversial to what extent it is actually effective (Seager et al. 2003; Miyasaka and Nakamura 2005, 2010; Kawai and Koshiro et al 2020). One reason for this is the difficulty in evaluating the influence of low clouds in the air-sea coupled system. Here, we evaluate the low-cloud feedback using an atmosphere-ocean general circulation model (AOGCM).

Recently, Miyamoto et al. (2021, 2022a) applied techniques of the Clouds On-Off Klimate Model Intercomparison Experiment (COOKIE; Stevens 2012; Voigt et al. 2021) to a fully coupled

AOGCM. Specifically, low-cloud radiative effect (CRE) was artificially removed regionally to evaluate specific low-cloud impacts. The simulations conducted for the South Indian Ocean demonstrated that low-cloud feedback is essential in the summertime subtropical Mascarene high (Miyamoto et al. 2021). Lowered SST by low clouds prevents the intertropical convergence zone (ITCZ) from expanding poleward, suppressing deep-convective precipitation on the poleward flank of the ITCZ. The resultant anomalous diabatic cooling reinforces the surface Mascarene high and promotes the WES feedback. By contrast, the low-cloud feedback is modest in winter, when the suppression of deep-convective precipitation by low clouds is less effective due to climatologically low SST (Miyamoto et al. 2022a).

This study applies the same methodology as in Miyamoto et al. (2021, 2022a) to the North Pacific. Figure 1 shows climatological annual-mean distributions of low-cloud fraction (LCF), SST, and surface winds over the northeastern Pacific (NEP). The subtropical high resides over the eastern portion of the basin, and the northeasterly trade winds blow on its southeastern flank. Over local minima of SST, LCF maximizes off the California coast. We examine not only the low-cloud impacts on the subtropical high and SST over the NEP but also their implications on the climate around Hawaii and the Kuroshio region.

The rest of the paper is organized as follows. Section 2 describes data and model experiments. Section 3 examines the low-cloud impacts on the subtropical high and SST over the NEP. Section 4 discusses implications on the climate in the Hawaii and Kuroshio regions. Section 5 summarizes the present study.

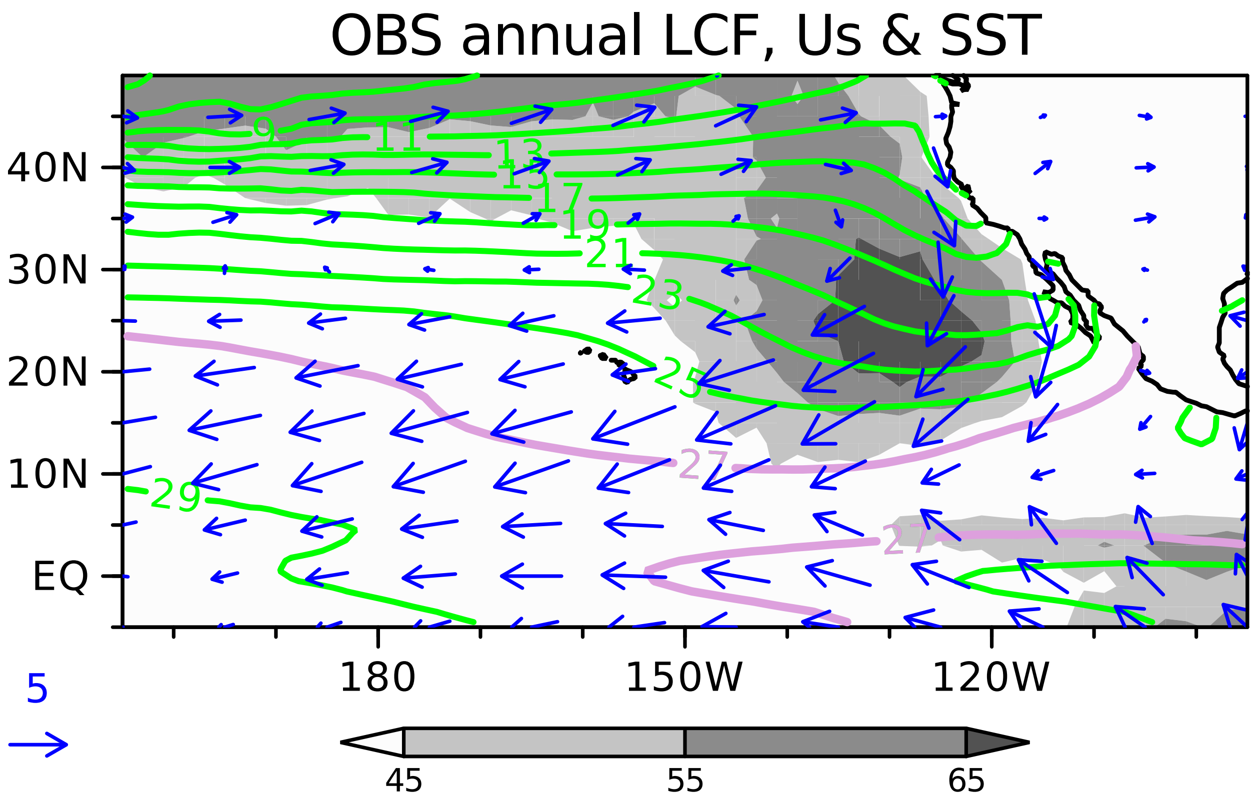

FIG. 1. Climatological annual-mean distributions of CALIPSO-GOCCP low-cloud fraction (%; color shaded as indicated at the bottom), OISST sea surface temperature (contoured for every 2°C in green with 27°C isotherms in purple), and JRA-55 surface winds (m s^{-1}; arrows with reference on the bottom). See Section 2b for details of the data.

2. Data and model experiments

a. Model experiments

Following Miyamoto et al. (2021, 2022a), radiative impacts of low clouds are evaluated by setting maritime cloud fraction to zero over a given geographical domain for radiation calculations in a fully coupled AOGCM, CM2.1 (Delworth et al. 2006). Its atmospheric component has $2.5^\circ \times 2^\circ$ resolution in longitude-latitude with 24 vertical levels. The resolution of the 50-level ocean model is 1° in both latitude and longitude, with meridional resolution equatorward of 30° progressively finer to 1/3° at the equator. We specify the domain [150°W-110°W, 16°N-32°N] in the subtropical NEP (black rectangles in Fig. 2; hereafter referred to as the NEP box), in which cloud fraction is set to zero artificially from the surface up to the 680-hPa level. After branched off from the same initial condition, both the low-cloud-off (CM_NoCRE) and control (CM_CTL) experiments are integrated for 110 years with the 1990-level radiative forcing. We analyze 100 years until November in the final year. A response to the low-cloud radiative effects simulated in CM2.1 is represented as CM_CTL−CM_NoCRE, which has the same sign as the low-cloud impacts. Within this analysis period, a model drift resulting from the low-cloud removal is found negligible: Radiative imbalance at the top of the atmosphere (TOA) in the last 100 years is 1.02 W m^{-2} in CM_CTL and 1.07 W m^{-2} in CM_NoCRE.

To isolate the SST influence simulated in CM2.1, we also conduct experiments with its atmospheric component, AM2.1. A control experiment (AM_CTL) is carried out with climatological SST and sea ice concentration in CM_CTL. One sensitivity experiment aimed at evaluating the local SST influence is AM_SSTAstNEP, where the prescribed SST is replaced by the CM_NoCRE climatology regionally over the NEP (180°-110°W, 10°N-32°N; note a slight difference from the NEP box). Another sensitivity experiment to isolate low-cloud impacts without SST changes is AM_NoCRE_SSTfixed, where radiative effects of Californian low clouds are eliminated as in CM_NoCRE but SST and sea ice are fixed to the CM_CTL climatology. Each of the AM2.1 experiments has been integrated for 51 years, and 50 years until the last November are analyzed. Table 1 summarizes the differences among the model experiments. The statistical significance of the model responses is determined with a Student's *t* test.

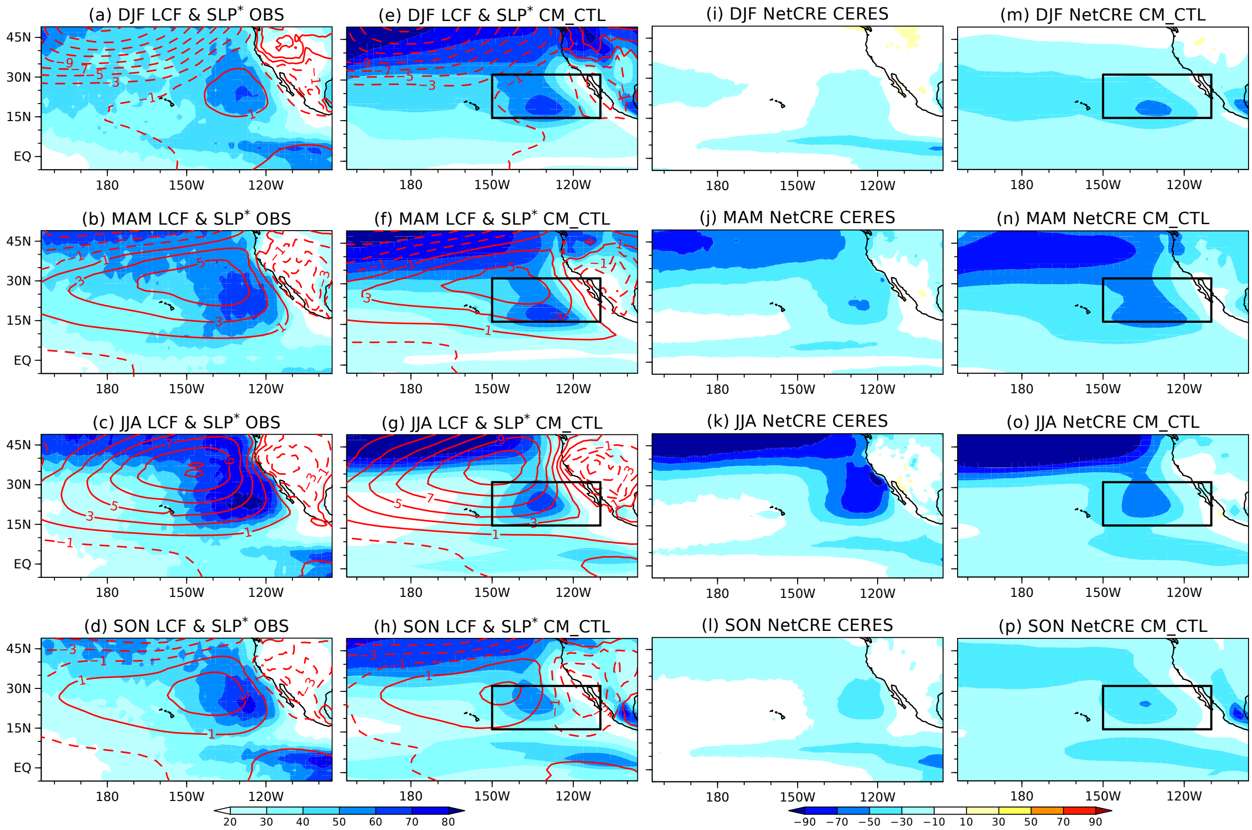

FIG. 2. (a)-(d) Climatological-mean distributions of CALIPSO-GOCCP LCF (%; color shaded as indicated at the bottom) and JRA-55 zonally asymmetric SLP (contoured for ±1, ±3, ±5 hPa; positive and negative values for solid and dashed lines, respectively) in (a) DJF, (b) MAM, (c) JJA, and (d) SON. (e)-(h) As in (a)-(d), respectively, but for the CM_CTL simulation. (i)-(l) As in (a)-(d), but for CERES-EBAF TOA net CRE (W m^{-2}). (m)-(p) As in (i)-(l), respectively, but for the CM_CTL simulation. Black box denotes the domain where low clouds are made transparent in CM_NoCRE.

b. Observational data

For the purpose of model validation, CM_CTL is compared with monthly observational data. We use the Japanese 55-year Reanalysis of the global atmosphere (JRA-55; Kobayashi et al. 2015; Harada et al. 2016) from 1979 to 2018 for sea-level pressure (SLP), the Clouds and the Earth's Radiant Energy System (CERES) Energy Balanced and Filled (EBAF) edition 4.1 (NASA/LARC/SD/ASDC 2019) from March 2000 to February 2020 for TOA radiative fluxes, the GCM-Oriented CALIPSO (*Cloud-Aerosol Lidar and Infrared Pathfinder Satellite Observations*)

TABLE 1. Overview of the CM2.1 (top two) and AM2.1 (bottom three) experiments.

	Radiative effects of Californian low clouds (150°W-110°W, 16°N-32°N)	Prescribed SST
CM_CTL	Active	—
CM_NoCRE	Inactive	—
AM_CTL	Active	Monthly climatology of CM_CTL
AM_SSTAstNEP	Active	Monthly climatology of CM_NoCRE over the northeastern Pacific (180°-110°W, 10°N-32°N) and CM_CTL elsewhere
AM_NoCRE_SSTfixed	Inactive	Monthly climatology of CM_CTL

Cloud Product (GOCCP) version 3 (Chepfer et al. 2010) from June 2006 to May 2017 for LCF, and the Optimum Interpolation SST V2 (OISST; Reynolds et al. 2002) from December 1981 through November 2017 for SST. The horizontal resolution is 1.25° in JRA55, 2° in CALIPSO-GOCCP, and 1° in CERES-EBAF and OISST.

Over the subtropical North Pacific, maximum negative CRE occurs off California associated with local LCF maximum (Fig. 2). These distributions compare well with the satellite observations, although their seasonal cycle in CM_CTL is weaker than in the observations. The North Pacific subtropical high seen as positive zonally asymmetric SLP is also well reproduced (Figs. 2a-h). As described in Wittenberg et al. (2006), CM2.1 is also skillful in simulating the tropical Pacific climate.

3. Low-cloud impacts on the northeastern Pacific climate

a. Coupled response of SST and surface winds

We begin with the annual-mean coupled response to radiative forcing of low clouds over the NEP. Figure 3 shows annual-mean response of SST, surface winds, and SLP. In the NEP box, negative SST response is up to -3°C (Fig. 3a) due to the negative CRE of low clouds (Figs. 2m-p). The SST response is not limited to the NEP box but extends well outside in the southwestward direction. The extension of the negative SST response is collocated with the strengthened northeasterly trade winds (Fig. 3a) associated with +2-hPa SLP response (Fig. 3b). This coupled pattern is reminiscent of the Pacific meridional mode (PMM; Chiang and Vimont 2004) and the joint WES-low cloud feedback as observed by Yang et al. (2022) in interannual variations (see also Xie 2023).

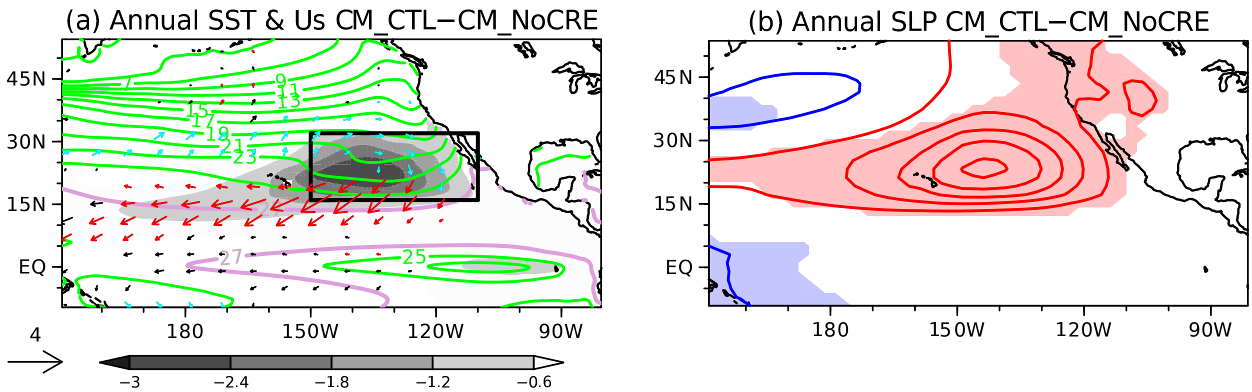

Fig. 3. Annual-mean response to CRE imposed in the black NEP box, represented by the difference defined as CM_CTL−CM_NoCRE. (a) SST (shaded as indicated at the bottom; only points with the 99% confidence for the difference are shaded) and surface winds (m s^{-1}; arrows with reference on the left; red and blue arrows signify increased and decreased scalar wind speed, respectively, with the 99% confidence for the difference). Superimposed with green contours is climatological-mean SST (every 2°C with 27 °C isotherms in purple) in CM_CTL. Black box denotes the domain where low clouds are made transparent in CM_NoCRE. (b) SLP (every 0.4 hPa; red and blue lines for positive and negative values, respectively; zero lines are omitted). Color shading indicates the 99% confidence for the difference.

Figures 4a-d show seasonal cycle of the coupled response, whereas Figs. 5a-b indicate ocean mixed-layer temperature (MLT; virtually equivalent to SST) and depth (MLD) in the NEP box. The negative SST response in the NEP box maximizes in summer (Figs. 4c and 5a), under the enhanced negative CRE in spring and summer (Figs. 2m-p) in combination with summertime shallow MLD (Fig. 5b).

A heat budget analysis for the ocean mixed layer substantiates the importance of CRE in the NEP box. As in Miyamoto et al. (2021), the budget equation may be cast as

$$\left(\frac{\partial \mathrm{MLT}}{\partial t}\right)' = \left(\frac{F}{\rho c_p H}\right)' + (\text{advection}) \tag{1}$$

where primes denote anomalies defined as CM_CTL−CM_NoCRE. In (1), F, ρ, and c_p denote the net downward surface heat flux (NSHF), sea-water density (1026 kg m^{-3}), and specific heat

(3990 J kg^{-1} °C^{-1}), respectively, whereas H represents MLD. A contribution of oceanic horizontal and vertical heat advection is evaluated as the residual. The first term on the RHS of (1) can be decomposed as

$$\left(\frac{F}{\rho c_p H}\right)' = \frac{F'}{\rho c_p \overline{H}} - \frac{\overline{F} \cdot H'}{\rho c_p \overline{H}^2} - \frac{F' \cdot H'}{\rho c_p \overline{H}^2} \tag{2}$$

where overbars signify monthly climatologies in CM_NoCRE. As shown by solid lines in Fig. 5c, the negative SST development into summer is attributable to the NSHF term whereas the oceanic advection term acts to stall the development. The early summer cooling is mostly attributable to anomalous NSHF (red dashed line in Fig. 5c) due to shortwave cooling by low clouds (purple line in Fig. 5d). The rest of the early summer cooling (Fig. 5c) is due to the slightly deeper MLD response (Fig. 5b) combined with the net climatological heating (second term on the RHS of (2)). The deeper MLD response is also consistent with the negative CRE of low clouds (Figs. 2m-p; Niiler and Kraus 1977).

While the total latent heat flux response acts to damp the SST cooling in the NEP box (Fig. 5c) due to its SST dependency (Xie et al. 2010), the trade winds (Figs. 4a-d) associated with the intensified subtropical high (Figs. 4e-h) are accelerated on the equatorward flank of the NEP box, promoting turbulent heat loss from the ocean by the augmented wind speed and cold-air advection. Furthermore, the negative SST response expands southwestward outside the NEP box, in accordance with the strengthened trade winds. This WES feedback is stronger in summer and autumn (Figs. 4c-d). Mechanisms of the surface wind response are detailed in the next subsection.

It is noteworthy that there are weak negative SST and surface easterly responses in the equatorial Pacific (Figs. 3 and 4a-d; the color map is shown in Fig. S1), reminiscent of the influence of the PMM on ENSO. As reviewed by Amaya (2019), the PMM's cool SST anomalies in the NEP can produce a La Niña-like SST pattern by forcing oceanic equatorial Kelvin waves and discharge of subsurface heat content. Indeed, impacts of the NEP low clouds on the equatorial Pacific have been identified by Yang et al. (2022) in interannual variations. Further investigation of the low-cloud impact on the equatorial Pacific is left for future work.

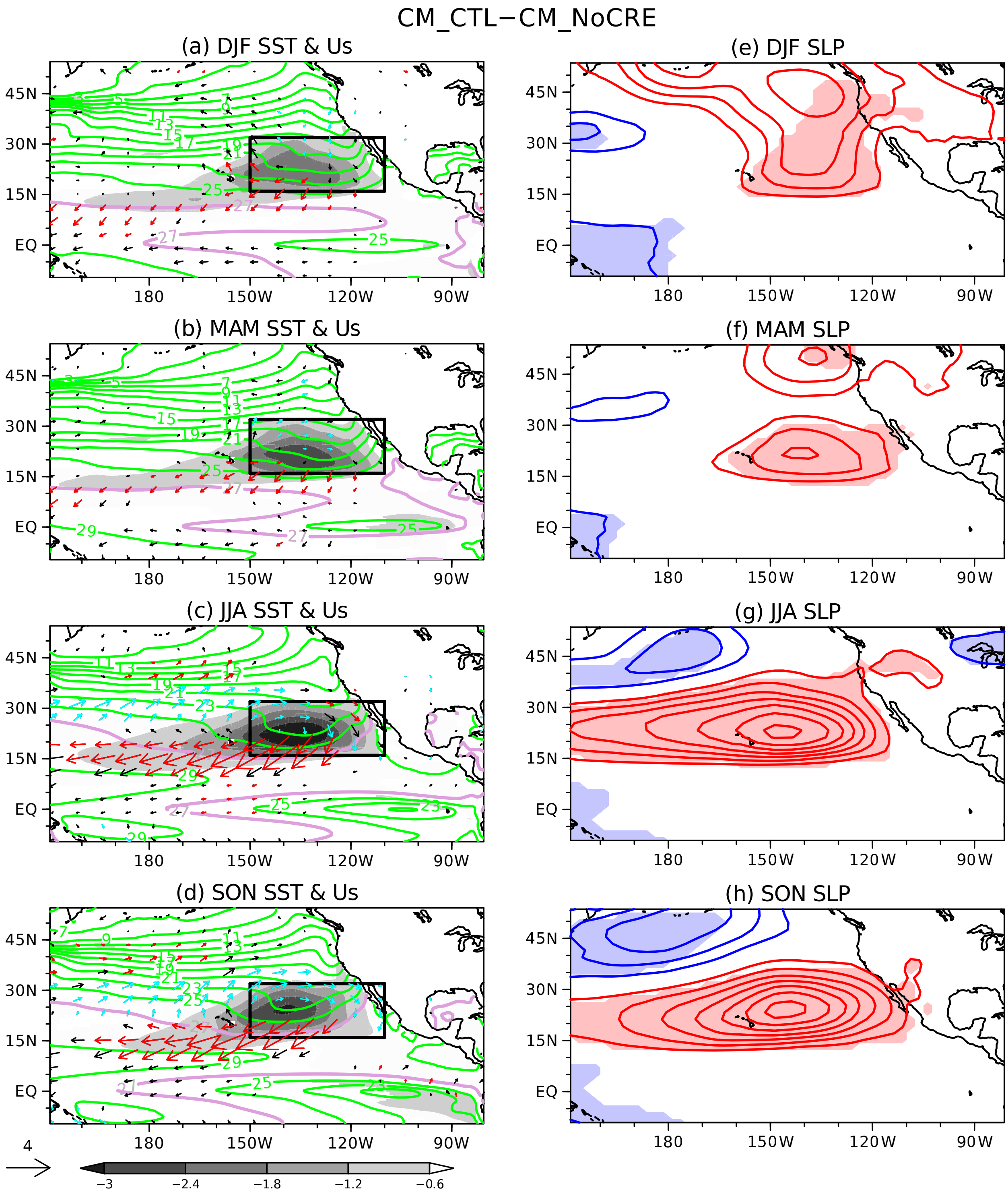

FIG. 4. As in Fig. 3, but for (a,e) DJF, (b,f) MAM, (c,g) JJA, and (d,h) SON.

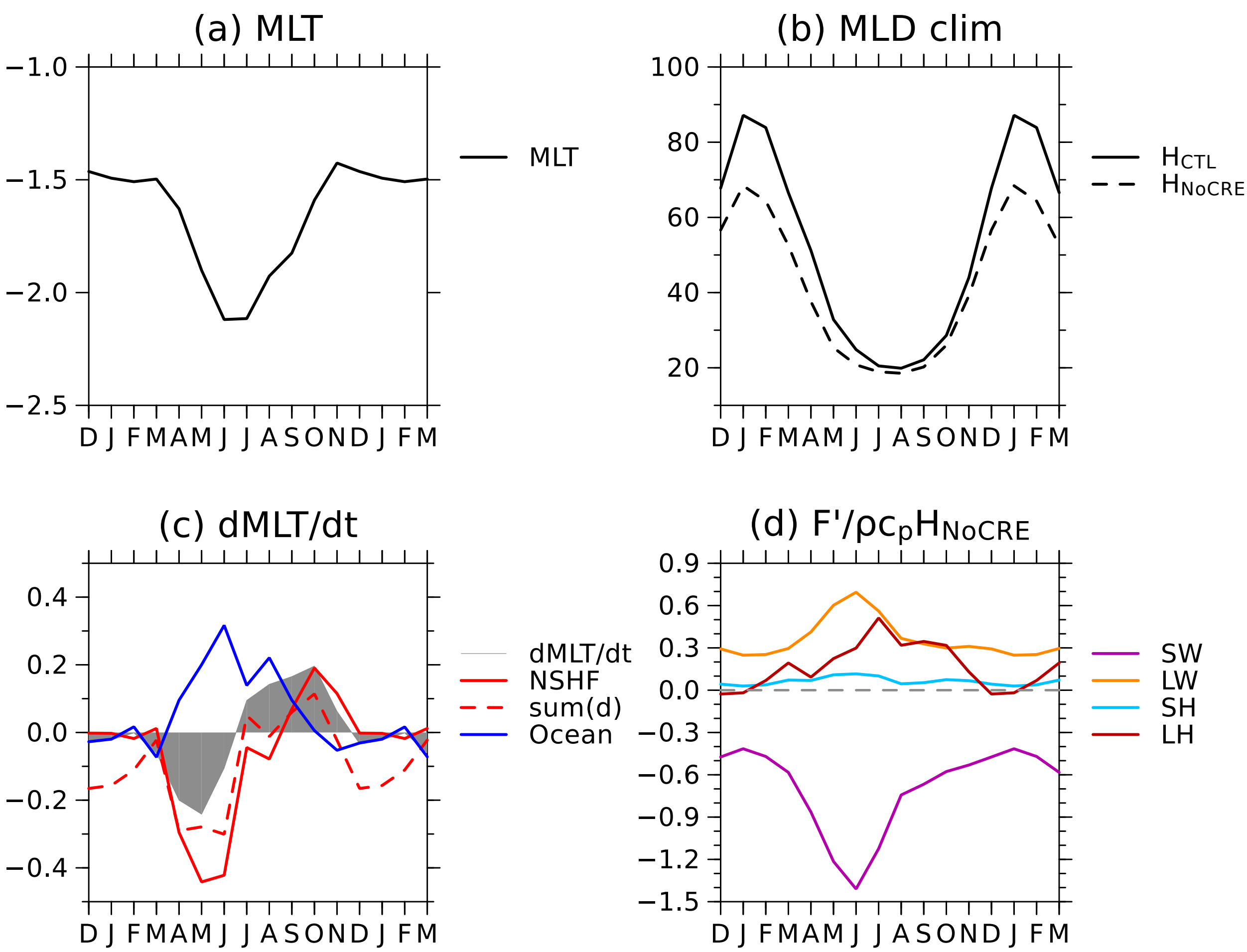

FIG. 5. (a) Area-mean difference of CM_CTL−CM_NoCRE in climatological-mean MLT (°C) in the NEP box (rectangles in Figs. 2-4). (b) Monthly climatology of MLD (m) in CM_CTL (solid) and CM_NoCRE (dashed). (c) As in (a), but for its anomalous rate of change (°C [30 day]$^{-1}$; grey filled line). Red and blue solid lines are NSHF and oceanic advection terms in (2), whereas red dashed line indicates the NSHF term with climatological-mean MLD ($F'/\rho c_p \overline{H}$). (d) As in red dashed line in (c), but for individual contributions from shortwave radiation (SW; purple line), longwave radiation (LW; orange line), sensible heat flux (SH; light blue line), and latent heat flux (LH; brown line) anomalies. The panels show one year starting from December, and additional four months ending in March. Note that MLD is defined as a depth at which buoyancy difference is 0.0003 m s^{-2} relative to the surface.

b. Response of the North Pacific subtropical high and its mechanism

Figures 4e-h show the seasonal-mean response of SLP in CM2.1. The subtropical center of the positive response is located at (150°-160°W, 20°-25°N) with minimum (~1.2 hPa) in spring and its maximum (~3 hPa) in summer and autumn. It coincides with the equatorward portion of the North Pacific subtropical high (Figs. 2e-h). We note that the winter response extends poleward, but its poleward portion exhibits weak statistical significance. The equatorward portion of the wintertime response is comparable to its springtime counterpart. Thus, the strong SLP response in summer and autumn is important for the annual-mean response (Fig. 3b).

Mechanisms of the SST forcing on the subtropical SLP response can be inferred from in-atmosphere diabatic heating. Figure 6 shows the vertically integrated response of diabatic heating, which is decomposed into condensation (Q_{precip}), vertical diffusion (Q_{vdf}), and radiation (Q_{rad}) components. The most prominent feature is seasonality in the Q_{precip} response (Figs. 6a-d). In summer and autumn, strong cooling response extends westward from the equatorward portion of the low-cloud deck, with narrower heating to the south. Since the vertically integrated Q_{precip} response is virtually equivalent to precipitation response, the summer and autumn responses indicate southward shift and shrink of the ITCZ, which is centered at 5°N-10°N (Wittenberg et al. 2006). Inducing a Matsuno-Gill-type baroclinic response (Matsuno 1966; Gill 1980; Kraucunas and Hartmann 2007), the diabatic cooling reinforces the subtropical high (Figs. 4g-h). An additional contribution comes from the moderate Q_{rad} cooling due to reduced deep-convective clouds of the ITCZ as well as increased low clouds (Figs. 6k-l). The Q_{vdf} response is weak throughout the year (Figs. 6e-h). In winter and spring, the pronounced Q_{precip} cooling diminishes (Figs. 6a-b) despite the comparable Q_{rad} remaining as in summer and autumn in the low-cloud region (Figs. 6i-j), This seasonality in the Q_{precip} cooling is consistent with the stronger positive SLP response in summer and autumn (Figs. 4e-h). Thus, the precipitation response is key to the seasonality in the subtropical anticyclonic response, as found for the Mascarene high over the South Indian Ocean (Miyamoto et al. 2021, 2022a).

This precipitation decrease is tied to the negative SST response. In Figs. 6a-d, superimposed with contours are isotherms of convective threshold SST (27°C for CM2.1 as revealed in Miyamoto et al. 2021), which corresponds to the threshold for active deep convection (Graham and Barnett 1987). In summer and autumn, the 27°C isotherm advances northward into the low-cloud region. The low-cloud-induced negative SST response (Figs. 4c-d) reduces precipitation along the ITCZ with the pronounced Q_{precip} decrease over the equatorward portion of the negative SST response (Figs. 6c-d). As the SST decrease extends into the deep tropics, the area of the negative Q_{precip} response also expands southwestward through Hawaii in summer and autumn. By contrast, displacement of the 27°C isotherms between the CM2.1 experiments is relatively small in winter and spring (Figs. 6a-b) due not only to the weaker SST response (Figs. 4a-b) but also to lower climatological SST after the winter solstice. This results in the much weaker Q_{precip} decrease in winter and spring.

The importance of the air-sea coupling over the NEP is substantiated by the AGCM experiments (Fig. 7). In response to the imposed SST cooling in the NEP, the difference of AM_CTL from AM_SSTAstNEP well reproduces the summertime enhanced subtropical high and decreased Q ($Q_{\text{precip}} + Q_{\text{vdf}} + Q_{\text{rad}}$) simulated in CM2.1 despite their overestimation (Figs. 7a and c). We confirmed that the remote influence of the equatorial Pacific SST anomalies (10°S-10°N) on the subtropical high is weak, as verified by another AM2.1 experiment forced with them (not shown). By contrast, based on the AM_CTL and AM_NoCRE_SSTfixed experiments, the CRE impact on summertime SLP without SST changes is quite weak (Fig. 7b) compared with its CM2.1 counterpart (Fig. 4g). This is consistent with the weak Q cooling due to the lack of the precipitation decrease south of the NEP box (Fig. 7d). Seasonal cycle of the SLP and Q responses in CM2.1 is also mostly explained by the NEP SST cooling (Figs. S2-4). Overall, our analysis demonstrates the importance of the subtropical air-sea coupling in the non-local low-cloud feedback.

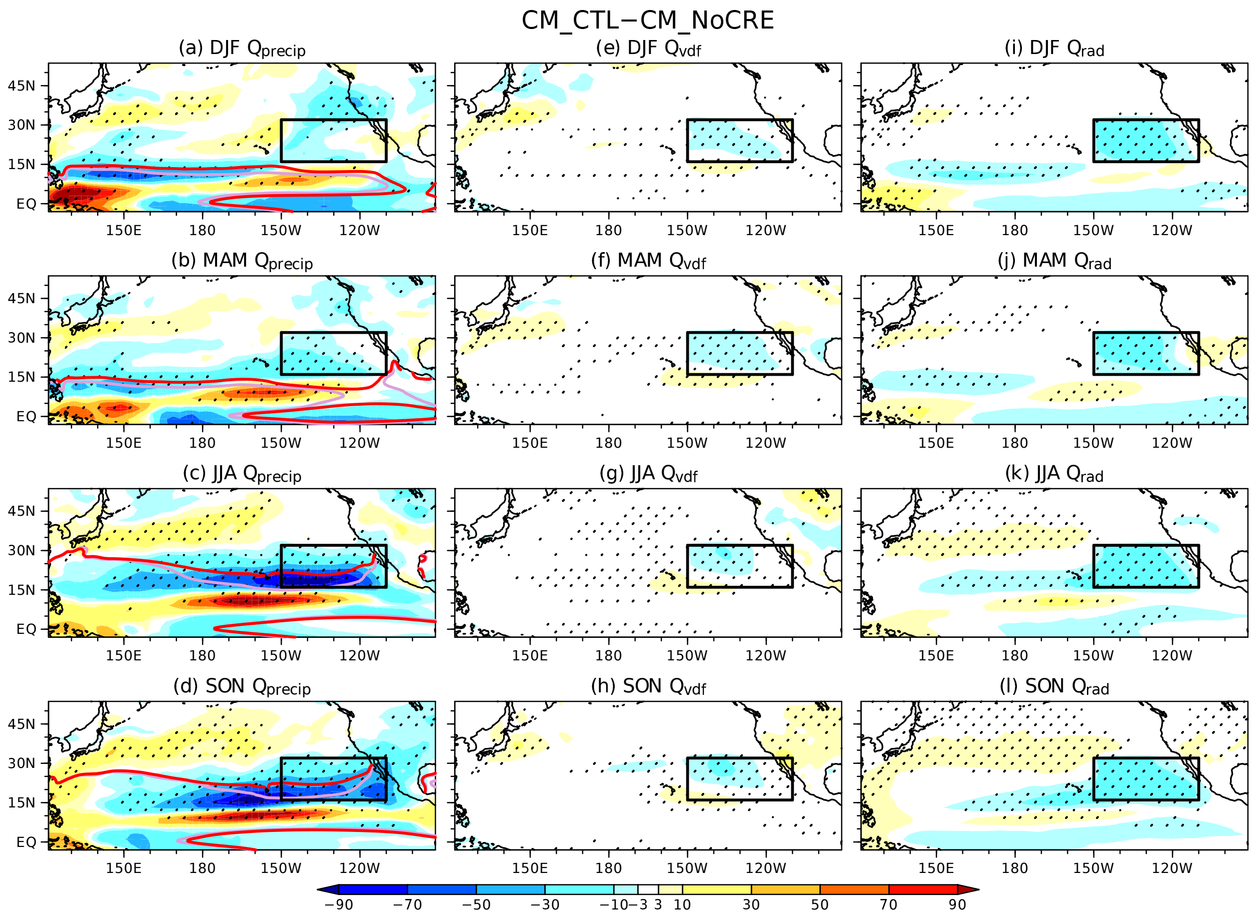

FIG. 6. Response to CRE imposed in the black NEP box, represented by the difference defined as CM_CTL−CM_NoCRE. (a)-(d) vertically integrated Q_{precip} (W m^{-2}; color shaded as indicated at the bottom) in (a) DJF, (b) MAM, (c) JJA, and (d) SON. (e)-(h) As in (a)-(d), respectively, but for Q_{vdf}. (i)-(l) As in (a)-(d), respectively, but for Q_{rad}. Stippling indicates the 99% confidence for the difference. Black box denotes the domain where low clouds are made transparent in CM_NoCRE. In (a)-(d), superimposed with red and purple contours are climatological-mean 27°C SST isotherms in CM_NoCRE and CM_CTL, respectively.

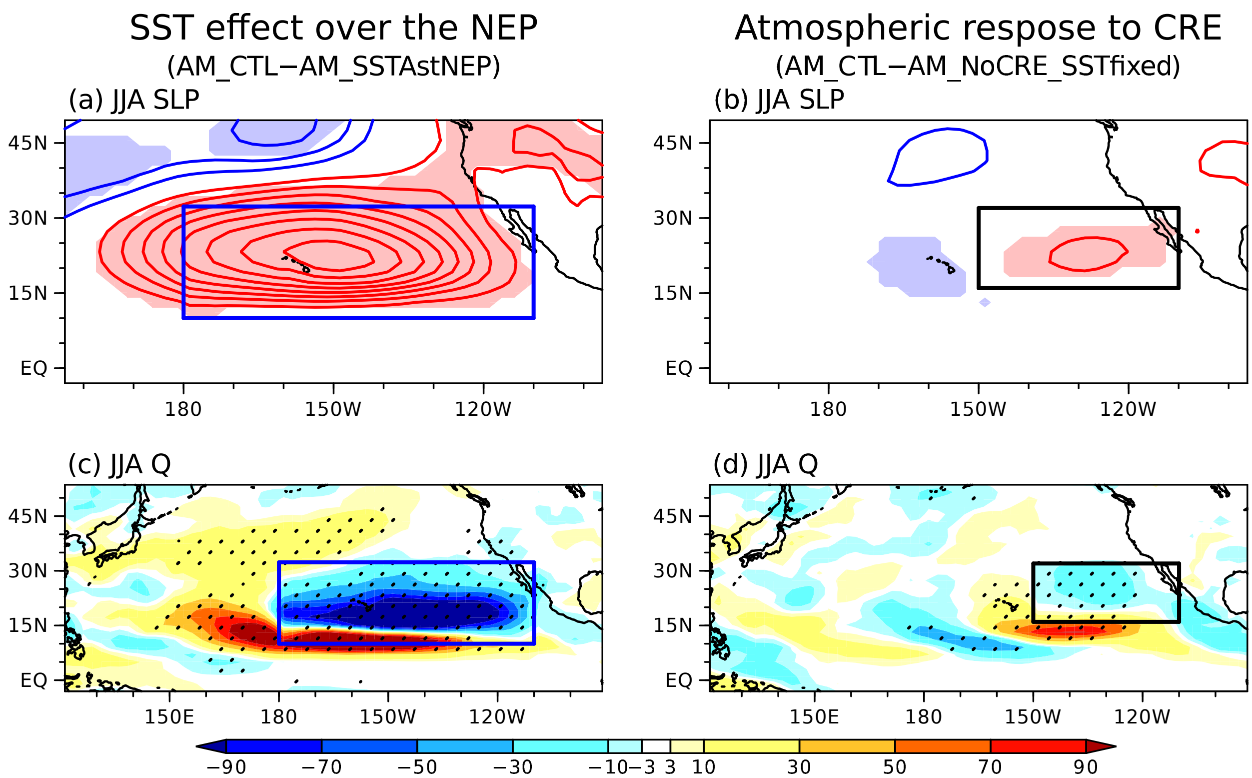

FIG. 7. AM2.1 response in JJA to (a)(c) anomalous SST over the NEP and (b)(d) CRE without SST changes. (a)(c) Differences defined as AM_CTL−AM_SSTAstNEP in climatological-mean (a) SLP (every 0.4 hPa; red and blue lines for positive and negative values, respectively; zero lines are omitted) and (c) $Q_{\mathrm{precip}} + Q_{\mathrm{vdf}} + Q_{\mathrm{rad}}$ (W m^{-2}; color shaded as indicated at the bottom). Color shading in (a) and stippling in (c) indicate the 99% confidence for the difference. Blue box denotes the domain where SST anomalies are prescribed in AM_SSTAstNEP. (b)(d) As in (a) and (c), respectively, but for AM_CTL−AM_NoCRE_SSTfixed. Black box denotes the domain where low clouds are transparent in AM_NoCRE_SSTfixed.

4. Discussions

a. Three-dimensional structure of the atmospheric response and its implication on tropical cyclone activity around Hawaii

The low-cloud impact extends into the upper troposphere. Here, we focus on the response from June through November (JJASON), i.e., the hurricane season over the NEP (Gray 1968). As shown in Fig. 8, CM2.1 simulates upper-tropospheric cyclonic response above the surface anticyclonic response over the summertime NEP. This first baroclinic structure as observed climatologically over the equatorward portion of the subtropical high (Miyasaka and Nakamura 2005; Nakamura et al. 2010), is consistent with the Matsuno-Gill-type response to the anomalous diabatic cooling (Figs. 6c,k). As shown in Fig. 8, the low-cloud impact reaches western Europe as wave trains from the NEP. Wave-activity flux, which is parallel to the group velocity of stationary Rossby waves (Takaya and Nakamura 2001), indicates the eastward wave propagation through subpolar North America and the Atlantic. This response is also reproduced by AM2.1 experiments forced by anomalous NEP SST (AM_CTL-AM_SSTAstNEP; figure not shown).

This first baroclinic structure corresponds to the enhanced vertical wind shear (VWS) on the southeastern flank of the subtropical high. Fig. 9a shows climatological VWS in JJASON, which is evaluated as a difference in monthly-mean zonal and meridional wind components between the 200-hPa and 850-hPa levels:

$$\mathrm{VWS} = \sqrt{(u_{200} - u_{850})^2 + (v_{200} - v_{850})^2}. \tag{3}$$

It features enhanced VWS between the near-surface easterlies and upper-tropospheric westerlies over Hawaii. Since VWS is destructive to tropical cyclones (Gray 1968; Tang and Emanuel 2012), this VWS prevents powerful hurricanes from hitting Hawaii.

Although the horizontal resolution of CM2.1 is insufficient to simulate tropical cyclones, it is beneficial to discuss the low-cloud impact on tropical cyclone genesis through environmental factors. The VWS response to CRE is shown in Fig. 9b. It exhibits positive VWS response on the southern flank of the upper-tropospheric cyclonic response, which accounts for ~30% of the climatological VWS around Hawaii in CM_CTL. The negative SST response also acts to decrease hurricane genesis over the NEP. The response of the maximum potential intensity for tropical cyclones (MPI; Emanuel 1988) shown in Fig. 9c features the negative MPI response that maximizes over the low-cloud regions and extends southwestward through Hawaii, in accordance with the negative SST response. The tropical cyclone genesis around Hawaii is further decreased by negative response of mid-tropospheric relative humidity (Fig. 9d). This drying is associated with anomalous subsidence owing to the suppression of deep-convective precipitation under the lowered SST, as discussed in the preceding section.

Collective influence of the environmental factors is evaluated with the genesis potential index (GPI; Camargo et al. 2007), which may be cast as

$$\mathrm{GPI} = |10^5\zeta|^{1.5}\left(\frac{\mathrm{RH}}{50}\right)^3\left(\frac{\mathrm{MPI}}{70}\right)^3(1+0.1\mathrm{VWS})^{-2} \tag{4}$$

where ζ, RH, and MPI are 850-hPa relative vorticity (s^{-1}), 600-hPa relative humidity (%), and the maximum potential intensity ($\mathrm{m\,s}^{-1}$). The GPI response shown in Fig. 9e features zonally elongated negative response maximized just south of Hawaii, which corresponds to reduced hurricane genesis. The relative contribution to this GPI response is derived by taking the natural logarithm of (4):

$$(\log\mathrm{GPI})' = 1.5\times10^5|\zeta|' + \frac{3}{50}\mathrm{RH}' + \frac{3}{70}\mathrm{MPI}' - 0.2\mathrm{VWS}'. \tag{5}$$

Decomposition of the GPI response based on (5) reveals that the RH, VWS, and MPI terms explain 42%, 30%, and 20% of the total response, respectively (Fig. 9f). The vorticity term plays a minor role. The analysis suggests that Californian low clouds act to protect Hawaii from hurricanes by lowering SST, drying the mid-troposphere, and increasing VWS.

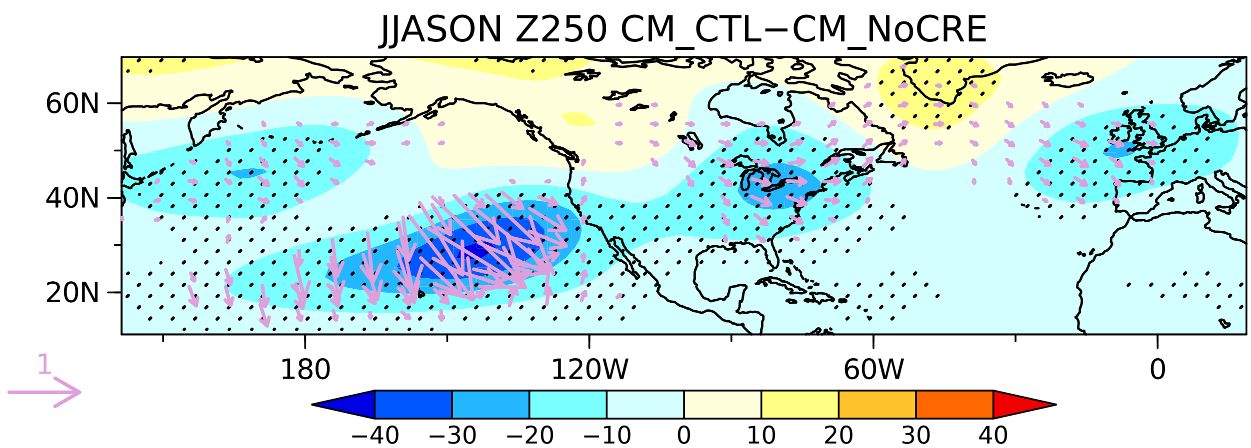

FIG. 8. JJASON 250-hPa geopotential height response to CRE imposed in the black NEP box, represented by the difference defined as CM_CTL−CM_NoCRE. Here, the global-mean response has been subtracted to eliminate signal of global cooling. Stippling indicates the 99% confidence for the difference. Superimposed with arrows is wave activity flux for stationary Rossby waves (m^2 s^{-2}; reference on the left) formulated by Takaya and Nakamura (2001). Onle fluxes above 0.05 m^2 s^{-2} in the westerly regions are drawn.

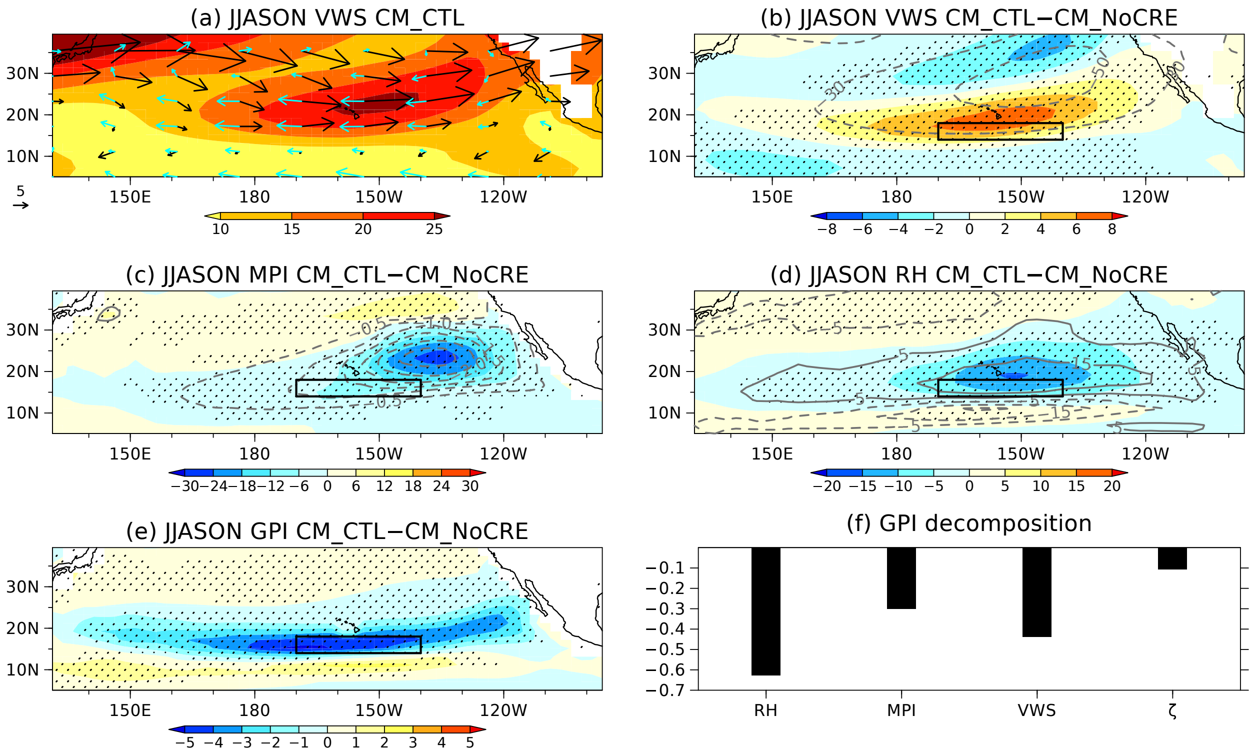

FIG. 9. (a) JJASON climatology of VWS (color shaded for every 5 m s^{-1}) in CM_CTL. Superimposed with black and blue arrows are JJASON climatologies of 200-hPa and 850-hPa winds in CM_CTL, respectively. (b) JJASON difference (defined as CM_CTL−CM_NoCRE) in VWS (color shaded for every 2 m s^{-1}) and 200-hPa geopotential height (contoured for ±10, ±30, ±50 ... m; positive and negative values for solid and dashed lines, respectively). (c) As in (b), but for MPI (color shaded for every 6 m/s) and SST (contoured for ±0.5, ±1, ±1.5 ... °C). (d) As in (b), but for 600-hPa relative humidity (color shaded for every 5%) and p-velocity (contoured ±5, ±15, ±25 ... hPa day^{-1}). (e) As in (b), but for GPI. (f) Decomposition of logGPI response to individual terms (RHS of (5)) averaged within black boxes in (b)-(e). In (b)-(e), stippling indicates the 99% confidence for the color-shaded difference.

b. Kuroshio acceleration and its influence on precipitation

The low-cloud impact extends farther into the northwestern Pacific through an ocean circulation change. Figure 10a shows the annual-mean CM2.1 response of wind stress curl and sea surface height (SSH). Associated with the positive SLP response (Figs. 4e-h), there is a strong anticyclonic wind stress curl response centered at 20°N, which is sandwiched meridionally by cyclonic responses (Fig. 10a). Forcing oceanic Rossby waves that propagate westward, this anticyclonic wind stress curl induces positive SSH response in the subtropical northwestern Pacific (Fig. 10a). This is indicative of acceleration of the subtropical gyre accompanied by the intensified North Equatorial Current and Kuroshio (Fig. 10b). The poleward and eastward current responses along Kuroshio and its extension account for ~30% of the CM_CTL current. Reflecting the enhanced heat transport, positive SST responses form along the accelerated Kuroshio and maximize its extension (Fig. 10b).

Recent studies have indicated that the Kuroshio Current system has significant impacts on the overlying atmosphere through heat and moisture supply (e.g., Kwon et al. 2010). As shown in Fig. 10c, upward turbulent heat fluxes are enhanced over the warm SST responses in the CM2.1 simulations, indicative of the oceanic forcing on the overlying atmosphere. Figure 10d shows the annual-mean response of precipitation and ∇^2SLP, the latter of which is proportional to surface wind convergence based on a marine boundary layer model (Lindzen and Nigam 1987; Minobe et al. 2008). Through hydrostatic pressure adjustments (Lindzen and Nigam 1987; Minobe et al. 2008), the enhanced sensible heating by the Kuroshio and its extension yields positive ∇^2SLP response locally (Fig. 10d). The associated enhancement of surface wind convergence as well as the augmented surface latent heat flux from the warmer SST increases precipitation by 10-20% of the CM_NoCRE climatology over the Kuroshio regions (Fig. 10d). This precipitation response is found in both warm and cold seasons (not shown). Such impacts of the warm Kuroshio SST on local precipitation have been identified in observations and reanalysis datasets (e.g., Tokinaga et al. 2009; Minobe et al. 2010; Masunaga et al. 2015, 2020). The Kuroshio warming may further energize atmospheric transient eddy activity (Taguchi et al. 2009) that acts to increase precipitation and to feed back onto the North Pacific subtropical high (Joh and Di Lorenzo 2019, and references therein), although it is not evident in our simulations (not shown) potentially due to the low resolution of the model. Thus, Californian low clouds can affect the climate in the Kuroshio region by accelerating the subtropical ocean gyre.

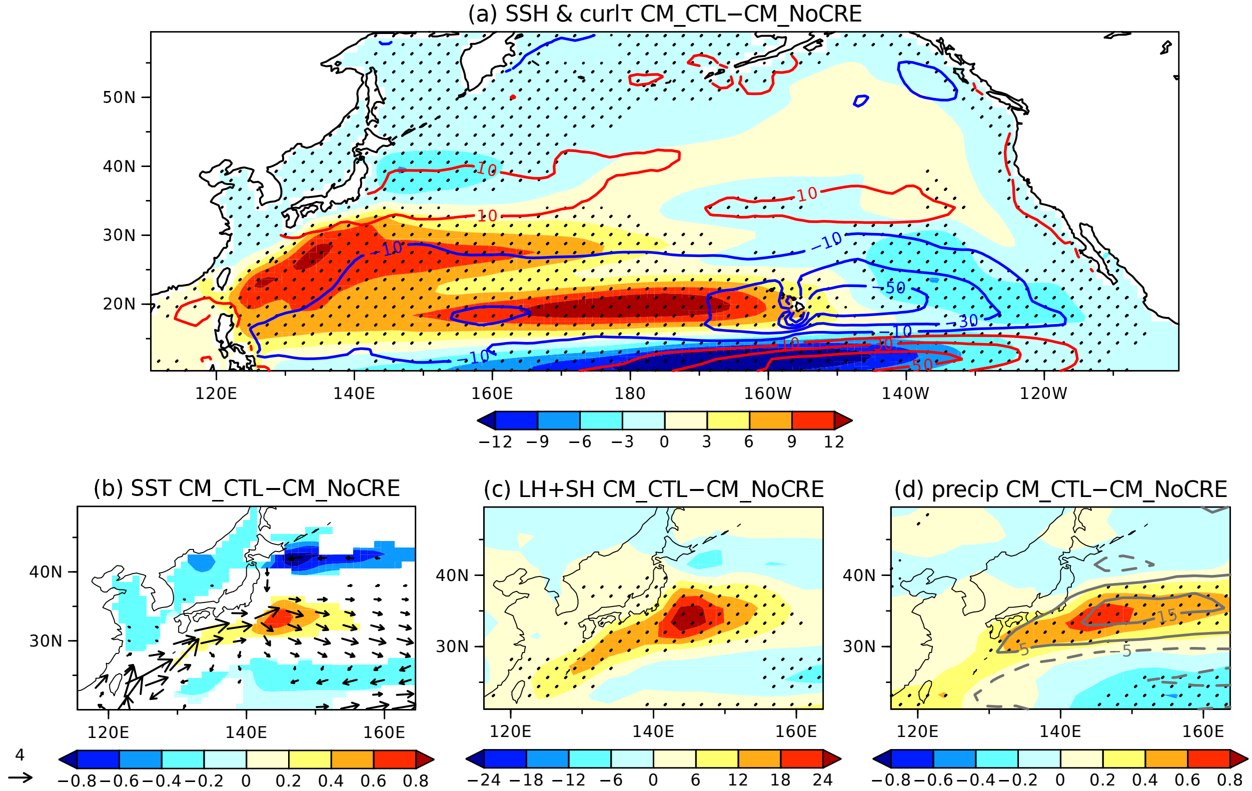

FIG. 10. Annual-mean response to CRE in the black NEP box, represented by the difference defined as CM_CTL−CM_NoCRE. (a) SSH (color shaded for every 3 cm) and wind stress curl (contoured for ±10, ±30, ±50 ... $\times10^{-9}$ N m^{-3}; positive and negative values for red and blue lines, respectively). (b) SST (color shaded for every 0.2 °C) and surface current (cm s^{-1}; arrows with reference on the left) with the 99% confidence for the difference. (c) Turbulent heat flux (sensible and latent heat fluxes combined; color shaded for every 6 W m^{-2}; positive values for upward flux). (d) Precipitation (color shaded for every mm day^{-1}) and ∇^2SLP (contoured for ±5, ±15, ±25 ... $\times10^{-13}$ hPa m^{-2}; positive and negative values for positive and dashed lines, respectively). In (a), (c), and (d), stippling indicates the 99% confidence for the color-shaded difference.

5. Concluding remarks

This study demonstrates the radiative impacts of low clouds off the California coast on the North Pacific climate system. A comparison of low-cloud-on-off AOGCM simulations reveals that the negative CRE of low clouds induces a negative SST response. Notably, the SST response is not limited to the low-cloud region but extends well outside in the southwestward direction. The extension of the negative SST response is collocated with the strengthened northeasterly trades associated with the enhanced subtropical high, indicative of the WES feedback.

The atmospheric responses are much stronger in boreal summer and autumn than in winter and spring as a result of air-sea interactions. The shortwave CRE strengthens toward summer due to large insolation. Combined with seasonally shallow MLD, the subtropical negative SST response maximizes in summer. This lowered SST suppresses deep-convective precipitation that would otherwise occur over seasonally high SST in the absence of CRE. Associated anomalous diabatic cooling induces the surface anticyclonic response as a baroclinic Matsuno-Gill pattern. The enhanced trade winds on its equatorward flank further cool SST through the WES feedback. Since climatological SST warming lags the summertime solstice, the precipitation and surface anticyclonic response remains strong in autumn as well, introducing spring-autumn asymmetries. No such enhancement of the atmospheric response in the warm seasons is simulated in the AGCM no-low-cloud experiments without SST changes, indicative of the crucial role of the air-sea interactions.

The aforementioned influence of Californian low clouds has implications on the climate over the Hawaii and Kuroshio regions. As a Matsuno-Gill-type response to the diabatic cooling, the surface anticyclonic response accompanies an upper-tropospheric cyclonic response. This first baroclinic structure augments vertical wind shear between the near-surface trades and upper-level westerlies around Hawaii. This result implies that low clouds act to prevent hurricanes from reaching Hawaii by enhancing environmental vertical wind shear and lowering regional SST. Our simulations also suggest a remote influence of low clouds through oceanic teleconnection. Input of anticyclonic wind stress leads to acceleration of the North Pacific subtropical ocean gyre and associated SST increase along the Kuroshio and its extension. Enhanced upward surface heat fluxes, which manifest forcing from the warmed Kuroshio and its extension, act to increase precipitation locally.

The summertime intensification of the low-cloud impact by seasonally high SST is similar to the low-cloud impact over the South Indian Ocean (Miyamoto et al. 2021, 2022a). This supports the notion suggested by Miyamoto et al. (2022a) that background climatologies are important for low-cloud impacts in climatology, and perhaps in climate variability and change. Although CM2.1 exhibits non-negligible low-cloud biases, the fact that the pronounced seasonality in the low-cloud impact is simulated despite the weaker seasonal cycle of low clouds in CM2.1 is a testament to its robustness. Nevertheless, it is important to evaluate the low-cloud impact in other climate models.

The low-cloud impacts simulated in our model may be operative in past and future climate change that accompanies persistent shortwave forcing of low clouds. For example, subtropical low clouds may decrease in response to CO_2 increase (e.g., Qu et al. 2014; Myers et al. 2021). Interestingly, our simulated climate without subtropical low clouds could happen in the past and future, since stratocumulus clouds have vulnerability and hysteresis against CO_2-level rises (Schneider et al. 2019). Our results have also implications for geoengineering by marine cloud brightening (e.g., Latham et al. 2008). Baughman et al. (2012) demonstrated that cloud brightening in the NEP low-cloud region yields non-local impacts with a southwestward extension of the SST cooling. Our analysis has revealed the dynamical mechanisms of this southwestward extension through the joint low cloud-WES feedback. Overall, our series of studies have demonstrated that low clouds play a key role in shaping a regional climate system by modulating subtropical air-sea interactions.

Acknowledgments. We thank Andrew Williams for his helpful input. This study is supported by the Japan Society for the Promotion of Science through Grants-in-Aid for Scientific Research (JP19H05702, JP19H05703, JP20H01970, and JP22H01292), by the Japanese Ministry of the Environment through the Environment Research and Technology Development Fund (JPMEERF20222002), by the Japanese Ministry of Education, Culture, Sports, Science and Technology (MEXT) programs for the ArCS II (JPMXD1420318865) and the advanced studies of climate change projection (JPMXD0722680395), by the Japan Science and Technology Agency through COI-NEXT (JPMJPF2013), and by the National Science Foundation (AGS-1934392).

Data availability statement. The authors can provide the model simulation data upon reasonable requests. The observational data used in this study are available online (JRA-55: `https://jra.kishou.go.jp/JRA-55/index_en.html`; CALIPSO-GOCCP; `https://climserv.ipsl.polytechnique.fr/cfmip-obs/`; CERES-EBAF: `https://ceres.larc.nasa.gov/data/`; OISST: `https://psl.noaa.gov`). The maximum potential intensity of tropical cyclones is calculated with pyPI (Gilford 2021).

References

Amaya, D. J., 2019: The Pacific meridional mode and ENSO: A review. *Curr. Clim. Change Rep.*, **5**, 296–307, https://doi.org/10.1007/s40641-019-00142-x.

Baughman, E., A. Gnanadesikan, A. Degaetano, and A. Adcroft, 2012: Investigation of the surface and circulation impacts of cloud-brightening geoengineering. *J. Climate*, **25**, 7527–7543, https://doi.org/10.1175/JCLI-D-11-00282.1.

Bony, S., and J.-L. Dufresne, 2005: Marine boundary layer clouds at the heart of tropical cloud feedback uncertainties in climate models. *Geophys. Res. Lett.*, **32**, L20806, https://doi.org/10.1029/2005GL023851.

Camargo, S. J., K. A. Emanuel, and A. H. Sobel, 2007: Use of a genesis potential index to diagnose ENSO effects on tropical cyclone genesis. *J. Climate*, **20**, 4819–4834, https://doi.org/10.1175/JCLI4282.1.

Chang, J. C. H., and D. J. Vimont, 2004: Analogous Pacific and Atlantic meridional modes of tropical atmosphere-ocean variability. *J. Climate*, **17**, 4143–4158, https://doi.org/10.1175/JCLI4953.1.

Chepfer, H., S. Bony, D. M. Winker, G. Cesana, J. Dufresne, P. Minnis, C. J. Stubenrauch, and S. Zeng, 2010: The GCM Oriented CALIPSO Cloud Product (CALIPSO-GOCCP). *J. Geophys. Res.*, **115**, D00H16, https://doi.org/10.1029/2009JD012251.

Clement, A. C., R. Burgman, and J. R. Norris, 2009: Observational and model evidence for positive low-level cloud feedback. *Science*, **325**, 460–464, https://doi.org/10.1126/science.1171255.

Delworth, T. L., and Coauthors, 2006: GFDL's CM2 global coupled climate models. Part I: Formulation and simulation characteristics. *J. Climate*, **19**, 643–674, https://doi.org/10.1175/JCLI3629.1.

Emanuel, K. A., 1988: The maximum intensity of hurricanes. *J. Atmos. Sci.*, **45**, 1143–1155, https://doi.org/10.1175/1520-0469(1988)045⟨1143:TMIOH⟩2.0.CO;2.

Gilford, D. M., 2021: pyPI (v1.3): Tropical cyclone potential intensity calculations in Python. *Geosci. Model Dev.*, **14**, 2351–2369, https://doi.org/10.5194/gmd-14-2351-2021.

Gill, A. E., 1980: Some simple solutions for heat-induced tropical circulation. *Quart. J. Roy. Meteor. Soc.*, **106**, 447–462, https://doi.org/10.1002/qj.49710644905.

Graham, N. E., and T. P. Barnett, 1987: Sea surface temperature, surface wind divergence, and convection over tropical oceans. *Science*, **30**, 657–659, https://doi.org/10.1126/science.238.4827.657.

Gray, W. M., 1968: Global view of the origin of tropical disturbances and storms. *Mon. Wea. Rev.*, **96**, 669–700, https://doi.org/10.1175/1520-0493(1968)096⟨0669:Gvotoo⟩2.0.Co;2.

Harada, Y., and Coauthors, 2016: The JRA-55 reanalysis: Representation of atmospheric circulation and climate variability. *J. Meteor. Soc. Japan*, **94**, 269–302, https://doi.org/10.2151/jmsj.2016-015.

Hartmann, D. L., M. E. Ockert-Bell, and M. L. Michelsen, 1992: The effect of cloud type on Earth's energy balance: Global analysis. *J. Climate*, **5**, 1281–1304, https://doi.org/10.1175/1520-0442(1992)005⟨1281:TEOCTO⟩2.0.CO;2.

Joh, Y., and E. Di Lorenzo, 2019: Interactions between Kuroshio extension and central tropical Pacific lead to preferred decadal-timescale oscillations in Pacific climate. *Sci. Rep.*, **9**, 13558, https://doi.org/10.1038/s41598-019-49927-y.

Klein, S. A., and D. L. Hartmann, 1993: The seasonal cycle of low stratiform clouds. *J. Climate*, **6**, 1587–1606, https://doi.org/10.1175/1520-0442(1993)006⟨1587:TSCOLS⟩2.0.CO;2.

Kobayashi, S., and Coauthors, 2015: The JRA-55 reanalysis: General specifications and basic characteristics. *J. Meteor. Soc. Japan*, **93**, 5–48, https://doi.org/10.2151/jmsj.2015-001.

Kraucunas, I., and D. L. Hartmann, 2007: Tropical stationary waves in a nonlinear shallow-water model with realistic basic states. *J. Atmos. Sci.*, **64**, 2540–2557, https://doi.org/10.1175/JAS3920.1.

Kwon, Y.-O., M. A. Alexander, N. A. Bond, C. Frankignoul, H. Nakamura, B. Qiu, and L. Thompson, 2010: Role of the Gulf Stream and Kuroshio-Oyashio systems in large-scale atmosphere-ocean interaction: A review. *J. Climate*, **23**, 3249–3281, https://doi.org/10.1175/2010JCLI3343.1.

Latham, J., and Coauthors, 2008: Global temperature stabilization via controlled albedo enhancement of low-level maritime clouds. *Philos. Trans. Roy. Soc. London A*, **366**, 3969–3987, https://doi.org/10.1098/rsta.2008.0137.

Lindzen, R. S., and S. Nigam, 1987: On the role of sea surface temperature gradients in forcing low-level winds and convergence in the tropics. *J. Atmos. Sci.*, **44**, 2418–2436, https://doi.org/10.1175/1520-0469(1987)044⟨2418:OTROSS⟩2.0.CO;2.

Masunaga, R., H. Nakamura, T. Miyasaka, K. Nishii, and Y. Tanimoto, 2015: Separation of climatological imprints of the Kuroshio Extension and Oyashio fronts on the wintertime atmospheric boundary layer: Their sensitivity to SST resolution prescribed for atmospheric reanalysis. *J. Climate*, **28**, 1764–1787, https://doi.org/10.1175/JCLI-D-14-00314.1.

Masunaga, R., H. Nakamura, B. Taguchi, and T. Miyasaka, 2020: Processes shaping the frontal-scale time-mean surface wind convergence patterns around the Gulf Stream and Agulhas Return Current in winter. *J. Climate*, **33**, 9083–9101, https://doi.org/10.1175/JCLI-D-19-0948.1.

Matsuno, T., 1966: Quasi-geostrophic motions in the equatorial area. *J. Meteor. Soc. Japan*, **44**, 25–43, https://doi.org/10.2151/jmsj1965.44.1_25.

Minobe, S., A. Kuwano-Yoshida, K. Nobumasa, S.-P. Xie, and R. J. Small, 2008: Influence of the Gulf Stream on the troposphere. *Nature*, **452**, 206–209, https://doi.org/10.1038/nature06690.

Minobe, S., M. Miyashita, A. Kuwano-Yoshida, H. Tokinaga, and S.-P. Xie, 2010: Atmospheric response to the Gulf Stream: Seasonal variations. *J. Climate*, **23**, 3699–3719, https://doi.org/10.1175/2010JCLI3359.1.

Miyamoto, A., H. Nakamura, and T. Miyasaka, 2018: Influence of the subtropical high and storm track on low-cloud fraction and its seasonality over the south Indian Ocean. *J. Climate*, **31**, 4017–4039, https://doi.org/10.1175/JCLI-D-17-0229.1.

Miyamoto, A., H. Nakamura, T. Miyasaka, and Y. Kosaka, 2021: Radiative impacts of low-level clouds on the summertime subtropical high in the south Indian Ocean simulated in a coupled general circulation model. *J. Climate*, **34**, 3991–4007, https://doi.org/10.1175/JCLI-D-20-0709.1.

Miyamoto, A., H. Nakamura, T. Miyasaka, and Y. Kosaka, 2022a: Wintertime weakening of low-cloud impacts on the subtropical high in the south Indian Ocean. *J. Climate*, **35**, 323–334, https://doi.org/10.1175/JCLI-D-21-0178.1.

Miyamoto, A., H. Nakamura, T. Miyasaka, Y. Kosaka, B. Taguchi, and K. Nishii, 2022b: Maintenance mechanisms of the wintertime subtropical high over the south Indian Ocean. *J. Climate*, **35**, 2989–3005, https://doi.org/10.1175/JCLI-D-21-0518.1.

Miyasaka, T., and H. Nakamura, 2005: Structure and formation mechanisms of the Northern Hemisphere summertime subtropical highs. *J. Climate*, **18**, 5046–5065, https://doi.org/10.1175/JCLI3599.1.

Miyasaka, T., and H. Nakamura, 2010: Structure and mechanisms of the Southern Hemisphere summertime subtropical anticyclones. *J. Climate*, **23**, 2115–2130, https://doi.org/10.1175/2009JCLI3008.1.

Myers, T. A., C. R. Mechoso, and M. J. DeFlorio, 2018: Coupling between marine boundary layer clouds and summer-to-summer sea surface temperature variability over the North Atlantic and Pacific. *Climate Dyn.*, **50**, 955–969, https://doi.org/10.1007/s00382-017-3651-8.

Myers, T. A., R. C. Scott, M. D. Zelinka, S. A. Klein, J. R. Norris, and P. M. Caldwell, 2021: Observational constraints on low cloud feedback reduce uncertainty of climate sensitivity. *Nat. Climate Change*, **11**, 501–507, https://doi.org/10.1038/s41558-021-01039-0.

Nakamura, H., T. Miyasaka, Y. Kosaka, K. Takaya, and M. Honda, 2010: Northern Hemisphere extratropical tropospheric planetary waves and their low-frequency variability: Their vertical structure and interaction with transient eddies and surface thermal contrasts. *Climate Dynamics: Why Does Climate Vary?*, D. Sun, and F. Bryan, Eds., *Geophys. Monogr.*, Vol. 189, Amer. Geophys. Union, 149–179, https://doi.org/10.1029/2008GM000789.

NASA/LARC/SD/ASDC, 2019: CERES Energy Balanced and Filled (EBAF) TOA and surface monthly means data in netCDF edition 4.1. NASA Langley Atmospheric Science Data Center DAAC, https://doi.org/10.5067/TERRA-AQUA/CERES/EBAF_L3B.004.1.

Niiler, P. P., and E. B. Kraus, 1977: One-dimensional models of the upper ocean. *Modelling and prediction of the upper layers of the ocean*, E. B. Kraus, Ed., Pergamon Press, 143–172.

Norris, J. R., and C. B. Leovy, 1994: Interannual variability in stratiform cloudiness and sea surface temperature. *J. Climate*, **7**, 1915–1925, https://doi.org/10.1175/1520-0442(1994)007⟨1915:IVISCA⟩2.0.CO;2.

Qu, X., A. Hall, S. A. Klein, and P. M. Caldwell, 2014: On the spread of changes in marine low cloud cover in climate model simulations of the 21st century. *Climate Dyn.*, **42**, 2603–2626, https://doi.org/10.1007/s00382-013-1945-z.

Reynolds, R. W., N. A. Rayner, T. M. Smith, D. C. Stokes, and W. Wang, 2002: An improved in situ and satellite SST analysis for climate. *J. Climate*, **15**, 1609–1625, https://doi.org/10.1175/1520-0442(2002)015⟨1609:AIISAS⟩2.0.CO;2.

Rodwell, M. J., and B. J. Hoskins, 2001: Subtropical anticyclones and summer monsoons. *J. Climate*, **14**, 3192–3211, https://doi.org/10.1175/1520-0442(2001)014⟨3192:SAASM⟩2.0.CO;2.

Schneider, T., C. M. Kaul, and K. G. Pressel, 2019: Possible climate transitions from breakup of stratocumulus decks under greenhouse warming. *Nat. Geosci.*, **12**, 163–167, https://doi.org/10.1038/s41561-019-0310-1.

Seager, R., R. Murtugudde, N. Naik, A. Clement, N. Gordon, and J. Miller, 2003: Air-sea interaction and the seasonal cycle of the subtropical anticyclones. *J. Climate*, **16**, 1948–1966, https://doi.org/10.1175/1520-0442(2003)016⟨1948:AIATSC⟩2.0.CO;2.

Seo, H., and Coauthors, 2023: Ocean mesoscale and frontal-scale ocean–atmosphere interactions and influence on large-scale climate: A review. *J. Climate*, **36**, 1981–2013, https://doi.org/10.1175/JCLI-D-21-0982.1.

Stevens, B., S. Bony, and M. J. Webb, 2012: Clouds On-Off Klimate Intercomparison Experiment (COOKIE). [Available online at http://hdl.handle.net/11858/00-001M-0000-0024-580A-3], 12 pp.

Taguchi, B., H. Nakamura, M. Nonaka, and S.-P. Xie, 2009: Influences of the Kuroshio/Oyashio Extensions on air-sea heat exchanges and storm track activity as revealed in regional atmospheric model simulations for the 2003/4 cold season. *J. Climate*, **22**, 6536–6560, https://doi.org/10.1175/2009JCLI2910.1.

Takaya, K., and H. Nakamura, 2001: A formulation of a phase-independent wave-activity flux for stationary and migratory quasigeostrophic eddies on a zonally varying basic flow. *J. Atmos. Sci.*, **58**, 608–627, https://doi.org/10.1175/1520-0469(2001)058⟨0608:AFOAPI⟩2.0.CO;2.

Tang, B., and K. Emanuel, 2012: A ventilation index for tropical cyclones. *BAMS*, **93**, 1901–1912, https://doi.org/10.1175/BAMS-D-11-00165.1.

Tokinaga, H., Y. Tanimoto, S.-P. Xie, T. Sampe, H. Tomita, and H. Ichikawa, 2009: Ocean frontal effects on the vertical development of clouds over the western North Pacific: In situ and satellite observations. *J. Climate*, **22**, 4241–4260, https://doi.org/10.1175/2009JCLI2763.1.

Voigt, A., N. Albern, P. Ceppi, K. Grise, Y. Li, and B. Medeiros, 2021: Clouds, radiation, and atmospheric circulation in the present-day climate and under climate change. *WIREs Clim. Change*, **12**, e694, https://doi.org/10.1002/wcc.694.

Wittenberg, A. T., A. Rosati, N.-C. Lau, and J. J. Ploshay, 2006: GFDL's CM2 global coupled climate models. Part III: Tropical Pacific climate and ENSO. *J. Climate*, **19**, 698–721, https://doi.org/10.1175/JCLI3631.1.

Wood, R., and C. S. Bretherton, 2006: On the relationship between stratiform low cloud cover and lower-tropospheric stability. *J. Climate*, **19**, 6425–6432, https://doi.org/10.1175/JCLI3988.1.

Xie, S.-P., 2023: Subtropical climate: Trade winds and low clouds. *Coupled Atmosphere-Ocean Dynamics: from El Nino to Climate Change*, Elsevier Science.

Xie, S.-P., and S. G. H. Philander, 1994: A coupled ocean-atmosphere model of relevance to the ITCZ in the eastern pacific. *Tellus*, **46A**, 340–350, https://doi.org/10.3402/tellusa.v46i4.15484.

Xie, S.-P., and Coauthors, 2007: A regional ocean-atmosphere model for eastern Pacific climate: Toward reducing tropical biases. *J. Climate*, **20**, 1504–1522, https://doi.org/10.1175/JCLI4080.1.

Yang, L., S.-P. Xie, S. S. P. Shen, J.-W. Liu, and Y.-T. Hwang, 2023: Low cloud-SST feedback over the subtropical Northeast Pacific and the remote effect on ENSO variability. *J. Climate*, **36**, 441–452, https://doi.org/10.1175/JCLI-D-21-0902.1.

Zelinka, M. D., T. A. Myers, D. T. McCoy, S. Po-Chedley, P. M. Caldwell, and P. Ceppi, 2020: Causes of higher climate sensitivity in CMIP6 models. *Geophys. Res. Lett.*, **47**, e2019GL085782, https://doi.org/10.1002/2015GL067416.